

Switching on ferromagnetic coupling by Mn/Sb antisite disorder in $\text{Mn}(\text{Bi}_{1-x}\text{Sb}_x)_4\text{Te}_7$: from electron-doped antiferromagnet to hole-doped ferrimagnet

Chaowei Hu,¹ Scott Mackey,¹ and Ni Ni^{1,*}

¹*Department of Physics and Astronomy and California NanoSystems Institute,
University of California, Los Angeles, CA 90095, USA*

(Dated: August 21, 2020)

We have systematically investigated the Sb-doping effect in the newly discovered Z_2 AFM topological insulator MnBi_4Te_7 through the transport and thermodynamic measurements and mapped out the doping-temperature phase diagram of $\text{Mn}(\text{Bi}_{1-x}\text{Sb}_x)_4\text{Te}_7$ ($x \leq 0.83$). The only Mn1 sublattice in MnBi_4Te_7 undergoes a paramagnetic to antiferromagnetic phase transition at $T_N = 12.7$ K. While T_N remains almost unchanged with doping, an additional antiferromagnetic to ferromagnetic transition of the Mn1 sublattice occurs at lower temperature T_c which monotonically increases and takes over T_N at $x = 0.68$. Meanwhile, upon doping, the Mn/Sb antisite disorders give rise to and strengthen the additional Mn2 and Mn3 sublattices. Despite no clear sign of the Mn2/Mn3-sublattice ordering at low dopings, at $x > 0.12$, in concert with the antiferromagnetic to ferromagnetic transition of the Mn1 sublattice, Mn2/Mn3 sublattices develop long-range order which couples antiferromagnetically to the Mn1 sublattice, leading to a ferrimagnetic ground state below T_c in this series. We argue the magnetic dilution and the ordering of the Mn2/Mn3 sublattices are responsible for the ferromagnetic switching of the Mn1 sublattice.

Introduction Magnetic topological material provides a great platform in discovering new topological states, such as the axion insulators, the magnetic Weyl semimetals, the Chern insulators and the 3D quantum anomalous Hall (QAH) insulators [1]. Emergent phenomena including QAH effect and quantized magnetoelectric effect (QME) have been proposed or observed in these phases, offering unprecedented technological opportunities to low-energy-consumption devices, quantum metrology and quantum computing [2–4]. Recently, natural heterostructural $\text{MnBi}_{2n}\text{Te}_{3n+1}$ ($n = 1, 2, 3, 4, 5$) series are shown to be intrinsic magnetic topological insulators (MTIs) with clean low-energy band structures [5–32]. They are made of alternating $n-1$ quintuple-layered (QL) blocks of $[\text{Bi}_2\text{Te}_3]$ and one septuple layer (SL) of $[\text{MnBi}_2\text{Te}_4]$. The great structural tunability and natural heterostructural nature of $\text{MnBi}_{2n}\text{Te}_{3n+1}$ have not only paved an avenue to realize various topological phenomena aforementioned [7, 8, 33], but also provided a rare and unique material family with tunable magnetic anisotropy and exchange interactions to study the interplay among magnetism, band topology, electron correlations and crystal structure.

MnBi_2Te_4 is a Z_2 AFM TI with A-type magnetic structure where spins antiferromagnetically couple along the c axis and ferromagnetically align in the ab plane. Despite that the bulk materials are heavily electron-doped, when MnBi_2Te_4 samples are gated to charge neutrality point in the 2D limit, zero-field and magnetic-field-induced QAH effects are observed at 1.5 K and up to 6.5 K [20, 21], respectively, which are orders larger than the previously reported values in $\text{Cr}_{0.15}(\text{Bi}_{0.1}\text{Sb}_{0.9})_{1.85}\text{Te}_3$ thin film [34]. By reducing the interlayer coupling with increasing n

and thus the interlayer Mn-Mn distance, $\text{MnBi}_{2n}\text{Te}_{3n+1}$ evolves from a Z_2 AFM TI with saturation fields of 8 T in MnBi_2Te_4 ($n = 1$) [9, 15, 35], 0.22 T in MnBi_4Te_7 ($n = 2$) [11] and 0.18 T in $\text{MnBi}_6\text{Te}_{10}$ ($n = 3$) [27], to a FM axion TI in $\text{MnBi}_8\text{Te}_{13}$ ($n = 4$) [12], making these high n members excellent candidates to show zero-field QAH and QME. Indeed, zero-field QAH effect was recently observed in a bulk crystal of $\text{MnBi}_{10}\text{Te}_{16}$ ($n = 5$) at elevated temperatures [13].

However, n is a discrete tuning parameter which cannot lead to continuous change of interlayer Mn-Mn coupling and thus provides less insight in the rich competition between various ground states. Meanwhile, chemical doping serves as a continuous tuning parameter. Compared to the case of trivial magnetic metal, in small-gap MTI $\text{MnBi}_{2n}\text{Te}_{3n+1}$, chemical doping may not only tune their magnetism but also their band topology and carrier density. Profound effects of Sb doping has been observed in $\text{Mn}(\text{Bi}_{1-x}\text{Sb}_x)_2\text{Te}_4$ single crystals. Besides an electron-carrier to hole-carrier change [18, 36], the series evolve from AFM MnBi_2Te_4 to ferrimagnetic MnSb_2Te_4 [36–38]. This evolution suggests complicated doping mechanism and defect chemistry in this series. Although single crystal neutron scattering study on MnBi_2Te_4 indicates Bi atoms substitute on Mn sites with no discernable Mn atoms on Bi sites [25], similar measurements on MnSb_2Te_4 reveal substantial antisite disorder between Mn and Sb 6c sites [37, 38], resulting in two Mn sublattices. The delicate energy-scale competition was demonstrated in a recent study on MnSb_2Te_4 [38]. While these two Mn sublattices always couple antiferromagnetically, in samples with slightly lower antisite disorder, each Mn sublattice orders antiferromagnetically; in samples with slightly higher antisite disorder, each Mn sublattice orders ferromagnetically.

Compared to MnBi_2Te_4 , the members with $n \geq 2$ has extra spacer $[\text{Bi}_2\text{Te}_3]$ layers and thus much larger Mn-

* Corresponding author: nini@physics.ucla.edu

Mn interlayer distances. Therefore, the AFM and FM ground states can be closer in energy, so these high n members are more sensitive to perturbations. Indeed, a recent study shows 30% of Sb doping makes $\text{MnBi}_6\text{Te}_{10}$ FM [39]. However, due to the lack of intermediate doping levels, it is unclear how the magnetism evolves from AFM to FM in $\text{MnBi}_6\text{Te}_{10}$. Here we report a systematic study of the effect of Sb doping on MnBi_4Te_7 .

Method Single crystals of $\text{Mn}(\text{Bi}_{1-x}\text{Sb}_x)_4\text{Te}_7$ (147 phase) with $x \leq 0.83$ were grown using the flux method [11, 12, 15]. The energy-dispersive-spectroscopy (EDX) data show the ratio of the real Sb concentration to the nominal Sb concentration is near 1.2 (Fig. 1(b)). Throughout the paper, x is defined as the real Sb doping level. Since each of the doped sample has a very narrow but different growth temperature window, to find the sweet spot of the furnace, similar growth strategy to the one for $\text{MnBi}_8\text{Te}_{13}$ was used [12]. Mn doped Bi_2Te_3 (023 phase) can intergrow with the targeted phase and may mask the intrinsic properties. Therefore, extra care were paid to select the best pieces for the study. First, x-ray diffraction at low angles for both the top and bottom (001) surfaces were measured to select the ones without the 023 phase on the surface. Then, a part of the selected piece was ground for the powder x-ray diffraction (PXRD) to further screen the samples without the 023 impurities. Finally, all measurements were performed on the same piece. We found no significant piece-to-piece variation in magnetic properties within each batch.

Results Both the PXRD and chemical analysis via EDX indicate that Sb was successfully doped into MnBi_4Te_7 . Figure 1(a) shows the PXRD patterns for various doping levels. All peaks can be indexed by the 147 phase. If there is significant 023 phase impurity, a clear hump will appear at the left shoulder of the (104) peak. As shown in the inset of Fig. 1(a), the 023 phase is indiscernible or less than 5% if there is. With Sb doping, the (005) peak roughly stays at the same angle while the (104) peak shifts moderately and the (110) peak shifts much to higher angles, indicating distinct in-plane and out-of-plane lattice response to the Sb doping. Figure 1(b) shows the doping-dependent lattice evolution. The lattice parameter a decreases linearly by 2% up to our highest doping level $x = 0.83$ while the lattice parameter c remains almost the same. This lattice evolution is similar to $\text{Mn}(\text{Bi}_{1-x}\text{Sb}_x)_2\text{Te}_4$ [36]. Ideally, Sb will just substitute Bi. However, due to the formation of Mn/Sb antisite [37, 38], Mn can occupy three different sites in the 147 phase. We denote the Mn atoms occupying the Mn site as Mn1 sublattice, the Mn atoms on the Bi site within the SL layer as Mn2 sublattice, and the Mn atoms occupying the Bi site in the spacer QL as Mn3 sublattice [11]. Since x-ray diffraction is not the most sensitive to the Mn/Sb site disorder, we could not get the detailed antisite disorder information reliably and future single-crystal neutron diffraction measurements are needed to settle down this issue.

Figure 2 summarizes the temperature-dependent sus-

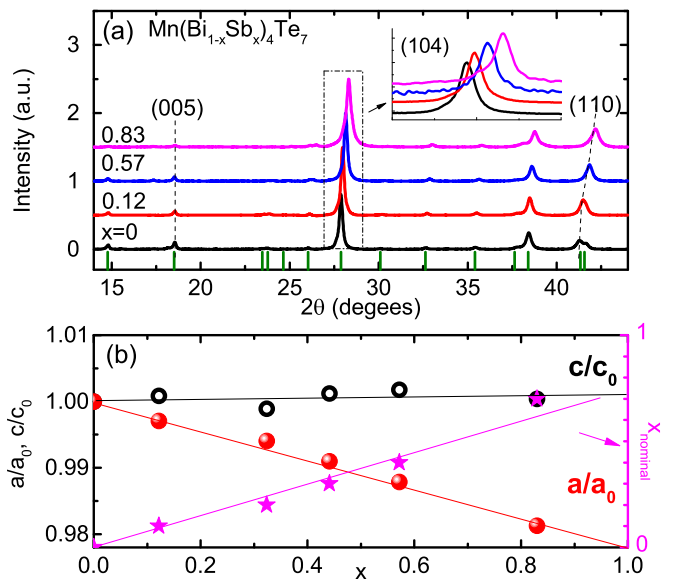


Figure 1. (a) PXRD of $\text{Mn}(\text{Bi}_{1-x}\text{Sb}_x)_4\text{Te}_7$ for the pieces for which the data in the paper were collected. The peak positions of the 147 phase are mar. Inset: the zoom-in plot of the (104) PXRD peak. (b) The doping-dependent relative lattice parameters a/a_0 , c/c_0 and nominal concentration x_{nominal} used in the growth. a_0 and c_0 are the lattice parameters for MnBi_4Te_7 .

ceptibility $\chi^{\parallel c}$ with $\text{H} \parallel c$, electrical resistivity with the current along the ab plane (ρ_{xx}) and c axis (ρ_{zz}), as well as the specific heat C_p for various dopings. For the $x = 0$ compound, as shown in Fig. 2, at 12.7 K, a sharp cusp in $\chi^{\parallel c}$ and a kink in C_p are observed, signaling a phase transition from paramagnetic (PM) to AFM. Furthermore, when it enters the ordered state at 12.7 K, the sudden increase of ρ_{zz} and the drop of ρ_{xx} are indicative of the gain of the spin-disorder scattering along the c axis and the loss of spin-disorder scattering in the ab plane. These distinct transport responses to the ordering indicate the spins align parallelly in the ab plane but anti-parallelly along the c axis. Indeed, this is consistent with the magnetic structure revealed by neutron scattering [15, 25].

For the $x = 0.12$ compound, in addition to a similar sharp cusp at 12.8 K in $\chi^{\parallel c}$ as in the $x = 0$ plot, a second transition occurs at 6.0 K marked by a sudden increase of $\chi^{\parallel c}$ and a large bifurcation in the ZFC and FC data. Associated with the transition at 12.8 K, ρ_{zz} increases sharply and ρ_{xx} drops. These behaviors are analogous to that in $x = 0$ sample, suggesting the A-type AFM between 12.8 K and 6.0 K. On the other hand, below 6.0 K, ρ_{zz} decreases sharply and ρ_{xx} shows a further slope change in lowering, indicating the loss of spin-disorder scattering along both the ab plane and the c axis and thus an AFM to FM transition at 6.0 K. This behavior is similar to the FM $\text{MnBi}_8\text{Te}_{10}$ [12]. While both phase transitions are clearly observed in the magnetic and transport data, only one specific heat anomaly shows up at 12.8 K.

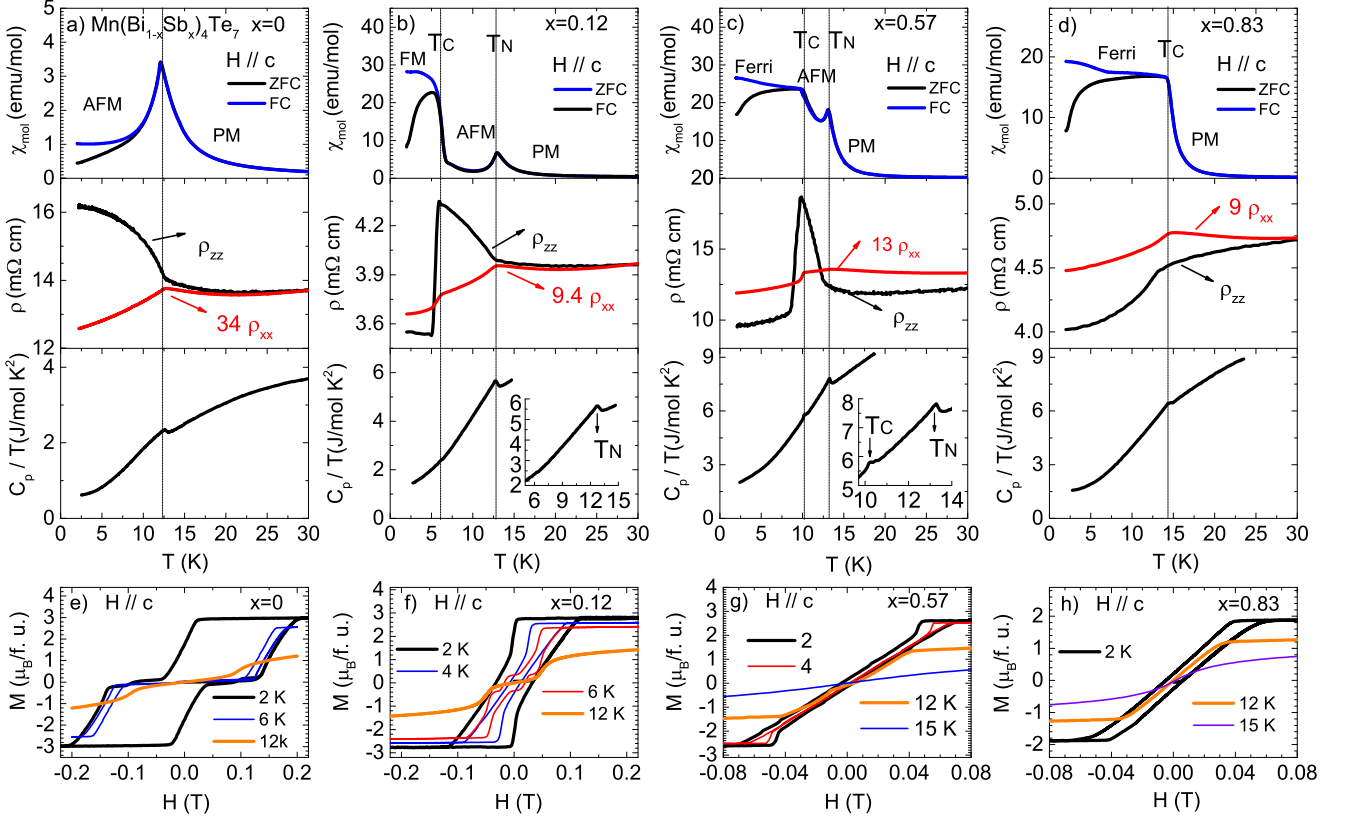


Figure 2. (a)-(d) For various doping concentration x , the temperature-dependent zero-field-cool (ZFC) and field-cool (FC) magnetic susceptibility with $H \parallel c$ ($\chi^{\parallel c}$, top panel), the temperature-dependent electrical resistivity (ρ_{xx} with the current along the ab plane; ρ_{zz} with the current along the c axis, middle panel), the temperature-dependent specific heat C_p (bottom panel), and the zoom-in plot of C_p near transition (inset). (e)-(h) For various doping x , the isothermal magnetization with $H \parallel c$ where c is the easy axis.

As shown in the zoom-in plot of C_p , no entropy release is discernible at 6.0 K. Usually, ordered-to-ordered magnetic phase transition will not cause entropy release [40]. Therefore, all these data evidence an AFM-to-FM phase transition of the Mn1 sublattice at 6.0 K upon cooling. We note due to the missing entropy release at 6.0 K, this phase transition is either unrelated to the Mn2 and Mn3 sublattices or the entropy release from PM to ordered phase of the Mn2 and Mn3 sublattices is too weak to be observed here.

For the $x = 0.57$ compound, it also has two phase transitions as shown in $\chi^{\parallel c}$, marked as a cusp at 13.3 K, a slope change at 10.2 K and a large bifurcation of the ZFC and FC data at 10.2 K. Furthermore, just like that in the $x = 0.12$ compound, upon cooling, the ρ_{zz} sharply increases at 13.3 K and then strongly drops below 10.2 K while the ρ_{xx} shows two slope changes in decreasing, indicating A-type AFM between 13.3 K and 10.2 K and dominant FM coupling below 10.2 K. However, unlike the case of $x = 0.12$, specific heat anomalies are observed at both transition temperatures, as clearly shown in the zoom-in plot. It is obvious that the entropy release at 13.3 K is much stronger than that at 10.2 K. Since it is

concluded from the $x = 0.12$ specific heat data that the phase transition from AFM to FM of the Mn1 sublattice will not release a discernible amount of entropy, the clear but small entropy release at 10.2 K in the $x = 0.57$ compound must be associated with the PM to magnetic ordering of the Mn2 and Mn3 sublattices.

For the $x = 0.83$ compound, only one phase transition is observed at 14.5 K. Upon cooling, this phase transition manifests itself at 14.5 K as a large bifurcation of the ZFC and FC $\chi^{\parallel c}$, an increase of the FC $\chi^{\parallel c}$ with a clear slope change, a sharp drop of the ρ_{zz} and ρ_{xx} , as well as a specific heat anomaly. The sharp decrease of both ρ_{zz} and ρ_{xx} arising from the reduced spin-disorder scattering along both the ab plane and c axis again indicates the dominant FM coupling below 14.5 K, similar to that in MnSb_2Te_4 with higher Sb/Mn antisite disorder [38].

While Figs. 2 (b)-(d) suggest dominant FM coupling at low temperatures for the $x = 0.12, 0.57$ and 0.83 compounds, to further identify how the three Mn sublattices couple magnetically to each other, the isothermal magnetization data are measured. As shown in Figs. 2(e)-(h), the saturation moment M_s right above the saturation fields is $3.0 \mu_B/\text{Mn}$ for $x = 0$, $2.8 \mu_B/\text{Mn}$ for $x = 0.12$, 2.2

μ_B/Mn for $x = 0.57$ and $1.9 \mu_B/\text{Mn}$ for $x = 0.83$. The data are summarized in Fig. 3(b) and we can see that M_s decreases linearly with x . The M_s of the $x = 0.12$ compound is very close to that of the parent compound, so the contribution of Mn2/Mn3 sublattices may be insignificant. However, those of the $x = 0.57$ and 0.83 compounds are way smaller. This is a sign of Mn2/Mn3 sublattices coupled antiferromagnetically to the Mn1 sublattice. That is, the ground state of the $x = 0.57$ and 0.83 compounds is ferrimagnetic with a FM Mn1 sublattice, similar to the case in MnSb_2Te_4 with larger Mn/Sb antisite disorder [38].

Furthermore, the envelope of the $M(H)$ curves are non-trivial. For the $x = 0.12$ compound, although we have concluded that the $x = 0.12$ compound is FM based on Fig. 2 (b), as the field sweeps from positive to negative, extra steps appear near 0 T in $M(H)$. This makes the curve a bow-tie shape and contrasts with a standard FM hysteresis loop. The bow-tie-shaped $M(H)$ can also be seen for the $x = 0.57$ sample at 2 K with a much smaller step at 0.04 T. This behavior is not unique to $\text{Mn}(\text{Bi}_{1-x}\text{Sb}_x)_4\text{Te}_7$, similar curves have also been observed in other systems with competing FM and AFM order [41]. Meanwhile, at 12 K, $M(H)$ data of the $x = 0.12$ compound become that of a typical AFM $M(H)$ curve with a spin-flip transition. There is also a tiny spin-flip transition near zero field in the $x = 0.57$ compound, but no such feature appears when $x = 0.83$. All these observations suggest partial AFM domains could exist below T_c in the $x = 0.12$ and 0.57 compounds with the overall FM ordering. This is an indication of how close the energy scales of the FM and AFM state are inside this family of compounds. We also noted that the multi-step feature of the $M(H)$ curve at 6 K for the $x = 0.12$ compound is reminiscent of that of the $\text{MnBi}_6\text{Te}_{10}$ compound [12]. Following our aforementioned discussion, this suggests small amount of FM domains exist in the AFM state of $\text{MnBi}_6\text{Te}_{10}$. Therefore, close energy scales of FM and AFM is universal in the $n \geq 2$ members of $\text{MnBi}_{2n}\text{Te}_{3n+1}$. This explains why there are some controversies on the nature of the ground states in MnBi_4Te_7 when different growth methods are used despite the first-principle calculations suggest an AFM ground state [11, 42, 43]. This is all because slight site defects are enough to tune the exchange energy to surrender one and boost the other.

Discussion We constructed a doping-temperature phase diagram of $\text{Mn}(\text{Bi}_{1-x}\text{Sb}_x)_4\text{Te}_7$ (Fig. 3) based on Fig. 2 and the magnetic/transport properties of a couple more doped compounds [44]. The competition between FM and AFM ground state of the Mn1 sublattice can be clearly visualized. For $x < 0.68$, the Mn1 sublattice undergoes a PM to A-type AFM at T_N , followed by an AFM to FM transition at T_c . There is no sign of magnetic ordering of the Mn2/Mn3 sublattices at $x = 0.12$, as suggested by the specific heat data. At higher dopings, the Mn2/Mn3 sublattices gradually become long-range ordered below T_c and antiferromagnetically cou-

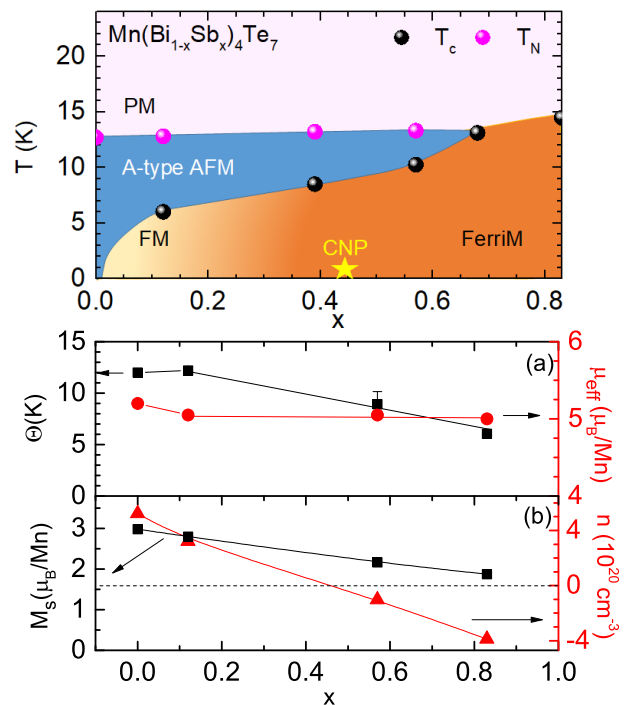


Figure 3. Top: The doping-temperature phase diagram of $\text{Mn}(\text{Bi}_{1-x}\text{Sb}_x)_4\text{Te}_7$. CNP: charge neutrality point. Bottom: (a): The doping-dependent Weiss temperature Θ and effective moment μ_{eff} with $H\parallel ab$. (b) The saturation moment M_s with $H\parallel c$ measured just above the saturation field and carrier density calculated from Hall resistivity at 20 K.

pled to the Mn1 sublattice, resulting in a ferrimagnetic phase transition at T_c . Furthermore, below $x = 0.68$, T_N remains unchanged at around 13 K with increasing x . Meanwhile, T_c shows a greater Sb-doping dependence where it quickly rises to 6 K near $x = 0.12$ and monotonically increases to 13.1 K at $x = 0.68$ and then slowly goes up to 14.5 K at $x = 0.83$.

Figure 3(a) summarizes the doping-dependent Weiss temperature Θ and effective moment μ_{eff} obtained by fitting the susceptibility data with $H\parallel ab$ from 75 K to 300 K [44]. Upon doping, there is little change in μ_{eff} while the Θ first remains almost the same up to $x = 0.12$, and then linearly decreases to 6.0 K at $x = 0.83$. This non-monotonic behavior further supports our picture of the magnetic evolution in this doping series, i. e., Mn2/Mn3 sublattices are insignificant to the magnetism at $x = 0.12$ and then couples antiferromagnetically with Mn1 with stronger extent at higher x , which leads to an unchanged Θ at $x = 0.12$ and decreasing Θ at $x > 0.12$.

The emergence and enhancement of T_c with x suggest that despite the unchanged Mn1-Mn1 interlayer distance, Sb doping reduces the energy cost for the Mn1 sublattice to go from the AFM state to FM state by weakening the AFM exchange interaction along the c axis. This can happen due to a combination of two mechanisms. One is through magnetic dilution, i.e., the lowering of Mn

occupancy on the Mn1 site caused by the increase of the antisite disorder with Sb doping; the other is due to the increasing coupling between the Mn1 and strengthened Mn2/Mn3 sublattices which may further stabilize the FM of the Mn1 sublattice.

Last but not least, Sb-doping is found to lower the electron concentration and eventually changes the carrier-type from electron to hole. A linear fitting with our data (Fig. 3(b)) yields a charge neutrality point near $x = 0.45$.

Conclusion The Mn/Sb antisite disorder in $\text{Mn}(\text{Bi}_{1-x}\text{Sb}_x)_4\text{Te}_7$ not only results in an electron-type to hole-type carrier change at around $x = 0.45$, but also progressively reduces the interlayer AFM exchange

interaction and thus results in an evolution of the ground state from a heavily electron-doped Z_2 antiferromagnet to a hole-doped ferrimagnet with the charge neutrality point around $x = 0.45$.

ACKNOWLEDGMENTS

Work at UCLA was supported by the U.S. Department of Energy (DOE), Office of Science, Office of Basic Energy Sciences under Award Number DE-SC0021117.

-
- [1] Y. Tokura, K. Yasuda, and A. Tsukazaki, *Nature Reviews Physics* **1**, 126 (2019).
- [2] K. He, Y. Wang, and Q.-K. Xue, *Annual Review of Condensed Matter Physics* **9**, 329 (2018).
- [3] C.-X. Liu, S.-C. Zhang, and X.-L. Qi, *Annual Review of Condensed Matter Physics* **7**, 301 (2016).
- [4] J. Wang, B. Lian, X.-L. Qi, and S.-C. Zhang, *Physical Review B* **92**, 081107 (2015).
- [5] D. S. Lee, T.-H. Kim, C.-H. Park, C.-Y. Chung, Y. S. Lim, W.-S. Seo, and H.-H. Park, *CrystEngComm* **15**, 5532 (2013).
- [6] E. Rienks, S. Wimmer, J. Sánchez Barriga, O. Caha, P. Mandal, J. Růžicka, A. Ney, H. Steiner, V. Volobuev, H. Groiss, *et al.*, *Nature* **576**, 423 (2019).
- [7] D. Zhang, M. Shi, T. Zhu, D. Xing, H. Zhang, and J. Wang, *Physical review letters* **122**, 206401 (2019).
- [8] J. Li, Y. Li, S. Du, Z. Wang, B.-L. Gu, S.-C. Zhang, K. He, W. Duan, and Y. Xu, *Science Advances* **5**, eaaw5685 (2019).
- [9] M. M. Otrokov, I. I. Klimovskikh, H. Bentmann, D. Estyunin, A. Zeugner, Z. S. Aliev, S. Gaß, A. Wolter, A. Koroleva, A. M. Shikin, *et al.*, *Nature* **576**, 416 (2019).
- [10] Z. S. Aliev, I. R. Amiraslanov, D. I. Nasonova, A. V. Shevelkov, N. A. Abdullayev, Z. A. Jahangirli, E. N. Orujlu, M. M. Otrokov, N. T. Mamedov, M. B. Babanly, *et al.*, *Journal of Alloys and Compounds* **789**, 443 (2019).
- [11] C. Hu, K. N. Gordon, P. Liu, J. Liu, X. Zhou, P. Hao, D. Narayan, E. Emmanouilidou, H. Sun, Y. Liu, *et al.*, *Nature communications* **11**, 1 (2020).
- [12] C. Hu, L. Ding, K. N. Gordon, B. Ghosh, H.-J. Tien, H. Li, A. G. Linn, S.-W. Lien, C.-Y. Huang, S. Mackey, *et al.*, *Science Advances* **6**, eaba4275 (2020).
- [13] H. Deng, Z. Chen, A. Wolloś, M. Konczykowski, K. Sobczak, J. Sitnicka, I. V. Fedorchenko, J. Borysiuk, T. Heider, M. Pluciński, K. Park, A. B. Georgescu, J. Cano, and L. Krusin Elbaum, *Nature Physics* (2020), 10.1038/s41567-020-0998-2.
- [14] Y. Gong, J. Guo, J. Li, K. Zhu, M. Liao, X. Liu, Q. Zhang, L. Gu, L. Tang, X. Feng, *et al.*, *Chinese Physics Letters* **36**, 076801 (2019).
- [15] J.-Q. Yan, Q. Zhang, T. Heitmann, Z. Huang, K. Chen, J.-G. Cheng, W. Wu, D. Vaknin, B. C. Sales, and R. J. McQueeney, *Physical Review Materials* **3**, 064202 (2019).
- [16] A. Zeugner, F. Nietschke, A. U. Wolter, S. Gaß, R. C. Vidal, T. R. Peixoto, D. Pohl, C. Damm, A. Lubk, R. Henrich, *et al.*, *Chemistry of Materials* **31**, 2795 (2019).
- [17] M. M. Otrokov, I. P. Rusinov, M. Blanco-Rey, M. Hoffmann, A. Y. Vyazovskaya, S. V. Eremeev, A. Ernst, P. M. Echenique, A. Arnau, and E. V. Chulkov, *Physical Review Letters* **122**, 107202 (2019).
- [18] B. Chen, F. Fei, D. Zhang, B. Zhang, W. Liu, S. Zhang, P. Wang, B. Wei, Y. Zhang, Z. Zuo, *et al.*, *Nature communications* **10**, 1 (2019).
- [19] Y.-J. Hao, P. Liu, Y. Feng, X.-M. Ma, E. F. Schwier, M. Arita, S. Kumar, C. Hu, M. Zeng, Y. Wang, *et al.*, *Physical Review X* **9**, 041038 (2019).
- [20] Y. Deng, Y. Yu, M. Z. Shi, Z. Guo, Z. Xu, J. Wang, X. H. Chen, and Y. Zhang, *Science* **367**, 895 (2020).
- [21] C. Liu, Y. Wang, H. Li, Y. Wu, Y. Li, J. Li, K. He, Y. Xu, J. Zhang, and Y. Wang, *Nature Materials* **19**, 522 (2020).
- [22] Y. Chen, L. Xu, J. Li, Y. Li, H. Wang, C. Zhang, H. Li, Y. Wu, A. Liang, C. Chen, *et al.*, *Physical Review X* **9**, 041040 (2019).
- [23] H. Li, S.-Y. Gao, S.-F. Duan, Y.-F. Xu, K.-J. Zhu, S.-J. Tian, J.-C. Gao, W.-H. Fan, Z.-C. Rao, J.-R. Huang, *et al.*, *Physical Review X* **9**, 041039 (2019).
- [24] B. Li, J.-Q. Yan, D. M. Pajerowski, E. Gordon, A.-M. Nedić, Y. Sizyuk, L. Ke, P. P. Orth, D. Vaknin, and R. J. McQueeney, *Physical review letters* **124**, 167204 (2020).
- [25] L. Ding, C. Hu, F. Ye, E. Feng, N. Ni, and H. Cao, *Physical Review B* **101**, 020412 (2020).
- [26] J.-Q. Yan, Y. Liu, D. Parker, Y. Wu, A. Aczel, M. Matsuda, M. McGuire, and B. Sales, *Physical Review Materials* **4**, 054202 (2020).
- [27] K. N. Gordon, H. Sun, C. Hu, A. G. Linn, H. Li, Y. Liu, P. Liu, S. Mackey, Q. Liu, N. Ni, *et al.*, arXiv preprint arXiv:1910.13943 (2019).
- [28] Y. Hu, L. Xu, M. Shi, A. Luo, S. Peng, Z. Wang, J. Ying, T. Wu, Z. Liu, C. Zhang, *et al.*, *Physical Review B* **101**, 161113 (2020).
- [29] L. Xu, Y. Mao, H. Wang, J. Li, Y. Chen, Y. Xia, Y. Li, J. Zhang, H. Zheng, K. Huang, *et al.*, arXiv preprint arXiv:1910.11014 (2019).
- [30] N. H. Jo, L.-L. Wang, R.-J. Slager, J. Yan, Y. Wu, K. Lee, B. Schruck, A. Vishwanath, and A. Kaminski, *Physical Review B* **102**, 045130 (2020).
- [31] S. Tian, S. Gao, S. Nie, Y. Qian, C. Gong, Y. Fu, H. Li, W. Fan, P. Zhang, T. Kondo, S. Shin, J. Adell,

- H. Fedderwitz, H. Ding, Z. Wang, T. Qian, and H. Lei, *Phys. Rev. B* **102**, 035144 (2020).
- [32] I. I. Klimovskikh, M. M. Otrokov, D. Estyunin, S. V. Ereemeev, S. O. Filnov, A. Koroleva, E. Shevchenko, V. Voroshnin, A. G. Rybkin, I. P. Rusinov, *et al.*, *npj Quantum Materials* **5**, 1 (2020).
- [33] H. Sun, B. Xia, Z. Chen, Y. Zhang, P. Liu, Q. Yao, H. Tang, Y. Zhao, H. Xu, and Q. Liu, *Physical review letters* **123**, 096401 (2019).
- [34] C.-Z. Chang, J. Zhang, X. Feng, J. Shen, Z. Zhang, M. Guo, K. Li, Y. Ou, P. Wei, L.-L. Wang, *et al.*, *Science* **340**, 167 (2013).
- [35] S. H. Lee, Y. Zhu, Y. Wang, L. Miao, T. Pillsbury, H. Yi, S. Kempinger, J. Hu, C. A. Heikes, P. Quarterman, *et al.*, *Physical Review Research* **1**, 012011 (2019).
- [36] J.-Q. Yan, S. Okamoto, M. A. McGuire, A. F. May, R. J. McQueeney, and B. C. Sales, *Physical Review B* **100**, 104409 (2019).
- [37] T. Murakami, Y. Nambu, T. Koretsune, G. Xiangyu, T. Yamamoto, C. M. Brown, and H. Kageyama, *Physical Review B* **100**, 195103 (2019).
- [38] Y. Liu, L.-L. Wang, Q. Zheng, Z. Huang, X. Wang, M. Chi, Y. Wu, B. C. Chakoumakos, M. A. McGuire, B. C. Sales, *et al.*, arXiv preprint arXiv:2007.12217 (2020).
- [39] J. Wu, F. Liu, C. Liu, Y. Wang, C. Li, Y. Lu, S. Matsuishi, and H. Hosono, *Advanced Materials* , 2001815 (2020).
- [40] E. Emmanouilidou, H. Cao, P. Tang, X. Gui, C. Hu, B. Shen, J. Wu, S.-C. Zhang, W. Xie, and N. Ni, *Physical Review B* **96**, 224405 (2017).
- [41] E. Lachman, R. A. Murphy, N. Maksimovic, R. Kealhofer, S. Haley, R. D. McDonald, J. R. Long, and J. G. Analytis, *Nature communications* **11**, 1 (2020).
- [42] J. Wu, F. Liu, M. Sasase, K. Ienaga, Y. Obata, R. Yukawa, K. Horiba, H. Kumigashira, S. Okuma, T. Inoshita, *et al.*, *Science advances* **5**, eaax9989 (2019).
- [43] R. C. Vidal, A. Zeugner, J. I. Facio, R. Ray, M. H. Haghighi, A. U. Wolter, L. T. C. Bohorquez, F. Caglieris, S. Moser, T. Figgemeier, *et al.*, *Physical Review X* **9**, 041065 (2019).
- [44] See Supplemental Material.